Radiative electron capture to the continuum in $U^{89+} + N_2$ collisions: Experiment and theory

P.-M. Hillenbrand,[1,*] S. Hagmann,[1] M. E. Groshev,[2] D. Banaś,[3] E. P. Benis,[4] C. Brandau,[1,5] E. De Filippo,[6] O. Forstner,[1,7] J. Glorius,[1] R. E. Grisenti,[1,8] A. Gumberidze,[1] D. L. Guo,[9] B. Hai,[9] M. O. Herdrich,[7,10] M. Lestinsky,[1] Yu. A. Litvinov,[1] E. V. Pagano,[11] N. Petridis,[1] M. S. Sanjari,[1] D. Schury,[1,5] U. Spillmann,[1] S. Trotsenko,[1] M. Vockert,[7,10] G. Weber,[10] V. A. Yerokhin,[12] and Th. Stöhlker[1,7,10]

[1]*GSI Helmholtzzentrum für Schwerionenforschung, D-64291 Darmstadt, Germany*
[2]*Department of Physics, St. Petersburg State University, 199034 St. Petersburg, Russia*
[3]*Institute of Physics, Jan Kochanowski University, PL-25-406 Kielce, Poland*
[4]*Department of Physics, University of Ioannina, 45110 Ioannina, Greece*
[5]*I. Physikalisches Institut, Justus-Liebig-Universität Giessen, D-35392 Giessen, Germany*
[6]*Istituto Nazionale di Fisica Nucleare, Sezione di Catania, I-95123 Catania, Italy*
[7]*Institut für Optik und Quantenelektronik, Friedrich-Schiller-Universität Jena, D-07743 Jena, Germany*
[8]*Institut für Kernphysik, Goethe-Universität, D-60438 Frankfurt am Main, Germany*
[9]*Institute of Modern Physics, Chinese Academy of Sciences, Lanzhou 730000, China*
[10]*Helmholtz-Institut Jena, D-07743 Jena, Germany*
[11]*Istituto Nazionale di Fisica Nucleare, Laboratori Nazionali del Sud, I-95123, Catania, Italy*
[12]*Peter the Great St. Petersburg Polytechnic University, 195251 St. Petersburg, Russia*

(Received 10 December 2019; accepted 29 January 2020; published 28 February 2020)

For U^{89+} projectiles colliding at a beam energy of 75.91 MeV/u with a N_2 target, we present a coincidence measurement between the cusp electrons emitted under an angle of 0° with respect to the projectile beam and the photons emitted under a polar angle of 90°. This radiative-electron-capture-to-continuum cusp directly probes the theory of electron-nucleus bremsstrahlung up to the high-energy endpoint in inverse kinematics. In the present study, significant improvement with respect to the experimental accuracy has been achieved, resulting in a finer agreement between experimental and theoretical results.

DOI: 10.1103/PhysRevA.101.022708

I. INTRODUCTION

Electron-nucleus bremsstrahlung is one of the fundamental collision processes that lead to the emission of x rays. In this process, the electron transfers a part of its initial energy E_i to the emitted photon E_γ, such that the final energy of the scattered electron is $E_f = E_i - E_\gamma$. The high-energy endpoint of electron-nucleus bremsstrahlung is the case where the photon carries away the highest possible energy, $E_\gamma \approx E_i$, and the outgoing electron populates a low-energy continuum state of the corresponding ion, $E_f \approx 0$. The high-energy endpoint has a finite cross section only for the case of an electron scattering off a bare nucleus or highly charged ion, while for electrons scattering off neutral atoms, the cross section converges to zero as E_γ approaches E_i [1,2].

From a theoretical side the high-energy endpoint of electron-nucleus bremsstrahlung is of particular fundamental interest due to its relation to the capture process of a free electron into a bound state of the ion under emission of a photon, termed radiative recombination, as pointed out already by Fano *et al.* [3–7] and Pratt *et al.* [8–10]. For nuclei with a large atomic number, an accurate theoretical description requires a fully relativistic representation of the initial and final continuum wave functions for the electron in the field of the nucleus, and an all-order treatment for the coupling of the electron with the radiation field of the emitted photon. First accurate numerical results were obtained in a comprehensive series of studies by Tseng and Pratt [1,2,11–14]. This method has been refined by Yerokhin *et al.* to calculate various combinations of differential cross sections and polarization correlations [15–17]. Corresponding experiments performed for high-energy electrons impinging on *neutral atomic* targets focused on the polarization of the emitted x rays, providing a good agreement with the theoretical calculations [18,19]. Recently, the next level of complexity has been reached by calculating electron-nucleus bremsstrahlung for incoming twisted electrons [20].

From an experimental side, the study of electron-nucleus bremsstrahlung in coincidence measurements of emitted electrons and photons for the case of energetic electrons impinging on *bare nuclei* at rest exceeds current technical capabilities. Most important, the high-energy endpoint cannot be studied in coincidence measurements of electrons impinging on an *atomic* target, as the scattered electron would reside at the target. A viable approach to study electron-nucleus bremsstrahlung at the high-energy endpoint is to use inverse

*p.m.hillenbrand@gsi.de

kinematics: A projectile beam of heavy bare ions collides with a target of quasifree electrons. The observables are the energy and the angle of the scattered electron and the emitted photon. This process is termed radiative electron capture to continuum (RECC), in analogy to the radiative electron capture (REC), which is the capture of a quasifree target electron into a bound state of the projectile ion under emission of a photon [21]. RECC was first investigated theoretically by Jakubassa-Amundsen [22–26], and first coincidence measurements were pioneered by Nofal *et al.* [27]. In Refs. [28,29], refined measurements were first compared to calculations of RECC based on the fully relativistic theory of Yerokhin *et al.* [15–17].

In the present study, we report new results for the RECC in collisions of

$$U^{89+} + N_2 \rightarrow U^{89+} + [N_2^+]^* + e^-(E_f, \vartheta_f) + \gamma(E_\gamma, \vartheta_\gamma)$$

at a projectile beam energy of 75.91 MeV/u. Here, N_2 serves as a target of quasifree electrons, since the molecular binding energies and the electron binding energies in the atom are negligible compared to the collision energy. The energy distribution of cusp electrons E_f, emitted under a laboratory polar angle of $\vartheta_f \approx 0^\circ$ with respect to the projectile beam was measured in coincidence with the photon emitted under $\vartheta_\gamma = 90^\circ$ with an energy of E_γ. The Li-like U^{89+} projectile ions are used in such experiments for the first time and thus the results are additive to those for U^{88+} projectile ions in similar collision energies reported in Ref. [28]. Moreover, few-electron ions allow for detecting the energy spectrum of the electron-loss-to-continuum (ELC) cusp, that serves as a diagnostic tool for the measurements. Detailed calculations for the RECC of the measured system were performed applying the fully relativistic approach mentioned above and compared to the measurements. The results of this paper represent a considerable improvement of the agreement between theory and experiment as compared to the results reported in Refs. [28,29]. Thus, the results can be considered as an important step towards an in-depth understanding of the RECC process.

The rest of this paper is organized as follows: In Sec. II the experimental method is presented. The theoretical Sec. III focuses on the relevant kinematics and transformations. The results are presented and discussed in Sec. IV. Throughout the rest of the paper, primed variables refer to projectile frame centered around the U^{89+} ion, while unprimed variables refer to the target frame centered around the N_2.

II. EXPERIMENT

A. Measurement

The experiment was performed at the experimental storage ring (ESR), which is part of the heavy-ion accelerator complex of the GSI Helmholtzzentrum für Schwerionenforschung in Darmstadt, Germany. Uranium ions were accelerated by the linear accelerator UNILAC and the synchrotron SIS18 to the desired beam energy. Before injection into the ESR, the beam passed a carbon stripper foil with a specific thickness of 29 mg/cm^2 in order to produce the charge state of U^{89+}. In the ESR, electron cooling was applied for a reduction of the ion beam momentum spread. The beam velocity of the stored U^{89+} beam was defined by the space-charge corrected electron cooler voltage of $E_0 = 41.64$ keV. While this is the kinetic energy of the electrons in the electron cooler defining the ion beam velocity, it is also the energy cusp electrons have at the continuum threshold, when their velocity is identical to the projectile velocity, $v_e = v_p$. The corresponding projectile kinetic energy was 75.91 MeV/u, the projectile velocity in units of speed of light was $\beta = v_p/c = 0.3808$, and the Lorentz factor was $\gamma = 1.081$.

After the initial electron cooling period, the U^{89+} beam was intersected with a supersonic gas-jet target of N_2. Electrons emitted from the interaction point under a polar angle of $\vartheta_f = 0^\circ - \vartheta_{\max}$ and an azimuthal angle of $\varphi_f = 0^\circ - 360^\circ$ with respect to the projectile beam were measured by the electron spectrometer, as described in Sec. II B. Photons emitted under a polar angle of $\vartheta_\gamma = 90^\circ$ were measured with a standard high-purity germanium detector. Furthermore, U^{90+} and U^{88+} projectiles, that had lost or captured one electron, respectively, were measured in corresponding particle detectors located downstream of the target. Further details of the experimental arrangement have been described in Refs. [28,30].

B. Electron spectrometer

The electron spectrometer is built up of two 60° dipole magnets, each with a bending radius of 229 mm, and an iron-free quadrupole triplet in between the two dipole magnets. The optics is arranged as double-bend achromat, where undesired nonlinear effects partially cancel out. The dipole magnets are focusing in the horizontal and the vertical plane, and the difference in the focal length of both planes is designed to be compensated by the quadrupole triplet. After the second dipole, slits are used to limit the horizontal aperture in the image plane of the interaction point, in order to suppress background on the subsequent electron detector. The electron detector, a combination of two microchannel plates (MCP) and a position sensitive delay-line anode, has an active diameter of 75 mm, and is sufficiently large to collect all transported electrons.

The optics of the electron spectrometer has been simulated using first-order transport matrices. These simulations were used to optimize the distances between the optical elements as well as the settings of the quadrupole triplet. Full three-dimensional tracking simulations have been outside of the scope of the present project.

The aperture of the spectrometer is limited by the radius of the beam pipe, which is at least 50 mm along the entire electron path. To first order, the angular acceptance is given by the distance from the interaction point to the optical entrance of the first dipole magnet, which is 790 mm. This results in a geometric polar acceptance angle of $\vartheta_{\max}^{\text{geo}} = 3.6^\circ$. However, the effective aperture may be smaller due to uncompensated nonlinear effects in the electron optics, which originate mainly from the fringe fields of the dipole magnets. Additionally, nonideal settings of the quadrupole triplet and slight misalignments may reduce the effective aperture. Furthermore, the horizontal and vertical acceptance, $\vartheta_{\max}^x$ and $\vartheta_{\max}^y$, respectively, might differ slightly, resulting in an effective angular acceptance of $\vartheta_{\max}^{\text{eff}} = \sqrt{\vartheta_{\max}^x \times \vartheta_{\max}^y}$. Based on the above,

we adopted the value of $\vartheta_{\max} = 3.3^\circ \pm 0.3^\circ$ in the following analysis.

For completeness purposes we discuss the possibility for field ionization of electrons from Rydberg states of the projectile ion, as this has been an issue for electrostatic zero-degree electron spectrometers [31,32]. We consider that the magnetic field of the first spectrometer dipole magnet may lead to field ionization of $U^{88+}(1s^2 2snl)$ projectile ions, that have captured a target electron into a highly excited nl state, as discussed in Ref. [27]. For $E_f = E_0$, the dipole magnets were operated at a field strength of 3.1 mT. At these conditions, Rydberg electrons with binding energies $E_n \lesssim 0.44$ eV were field ionized, corresponding to Rydberg states $n \gtrsim 495$. Considering the energy range of emitted electrons relevant here, we have no reason to argue that field ionization perturbs the measured electron distribution in the present experiment.

C. Data analysis

In order to measure the triple-differential cross section $d^3\sigma/dE_f d\Omega_f d\Omega_\gamma$ as a function of the electron kinetic energy E_f, the number of background-corrected events for electrons detected in coincidence with a bremsstrahlung photon, $N_{e\wedge\gamma}$, was normalized to the integrated luminosity $L_{\rm int}$ at each electron spectrometer setting of E_f. The value of $L_{\rm int}$ was determined on a relative scale by the number of ionized U^{90+} ions detected with full efficiency in a particle detector downstream from the interaction point.

For each measured value of E_f, the experimentally derived cross section is given by [28]

$$\left.\frac{d^3\sigma^{\rm RECC}}{dE_f d\Omega_f d\Omega_\gamma}\right|_{\vartheta_f=0^\circ} = \frac{N_{e\wedge\gamma}}{L_{\rm int}} \frac{1}{\epsilon_e \Delta\Omega_e} \frac{1}{\epsilon_\gamma \Delta\Omega_\gamma} \times \frac{E_f + m_e c^2}{E_f^2 + 2E_f m_e c^2} \frac{1}{\Delta p_e/p_e}. \quad (1)$$

The electron detection efficiency of the MCP detector ϵ_e was assumed to be energy independent within the relevant energy range. The energy dependency in the efficiency of the x-ray detector, $\epsilon_\gamma(E_\gamma)$, was measured with calibrated radioactive sources. The solid angle of the x-ray detector mounted at $\vartheta_\gamma = 90^\circ$ was $\Delta\Omega_\gamma = 0.34\% \times 4\pi$, and the solid angle for the electrons was $\Delta\Omega_e = \pi\vartheta_{\max}^2$ with $\vartheta_{\max}$ as discussed in Sec. II B. The relative momentum acceptance of the spectrometer, $\Delta p_e/p_e = 2\%$, was constant across the measured momentum range. The energy factor with the electron rest energy $m_e c^2$ includes both the conversion of momentum-differential to energy-differential cross sections, dp_e/dE_f, and the dispersion correction, $1/p_e(\Delta p_e/p_e)$, i.e., the increasing absolute momentum acceptance with increasing momentum.

In the present analysis, the cross sections were evaluated according to Eq. (1) on a relative scale, due to large uncertainties in the absolute value of the detection efficiencies, and normalized to theory by multiplication with a fitted constant. Statistical error bars were calculated from $N_{e\wedge\gamma}$ taking into account the statistical error of the background correction.

At each setting of the electron spectrometer, the magnetic fields of the dipole magnets were measured by hall probes. These magnetic fields are proportional to the momentum of transmitted electrons. The momentum axis was converted into an energy axis. Then the energy axis was calibrated using the reaction,

$$U^{89+}(1s^2 2s) + N_2 \rightarrow U^{90+}(1s^2) + [N_2]^* + e^-,$$

which was measured in parallel through a coincidence detection of the zero-degree electron and the ionized U^{90+} projectile. For this collision system, the energy distribution of this ELC cusp is symmetric with respect to E_0 for energies E_f close to E_0 [30]. According to the width of the symmetric ELC cusp, the energy calibration was determined on an accuracy level of $|\Delta E_f/E_f| < 1\%$.

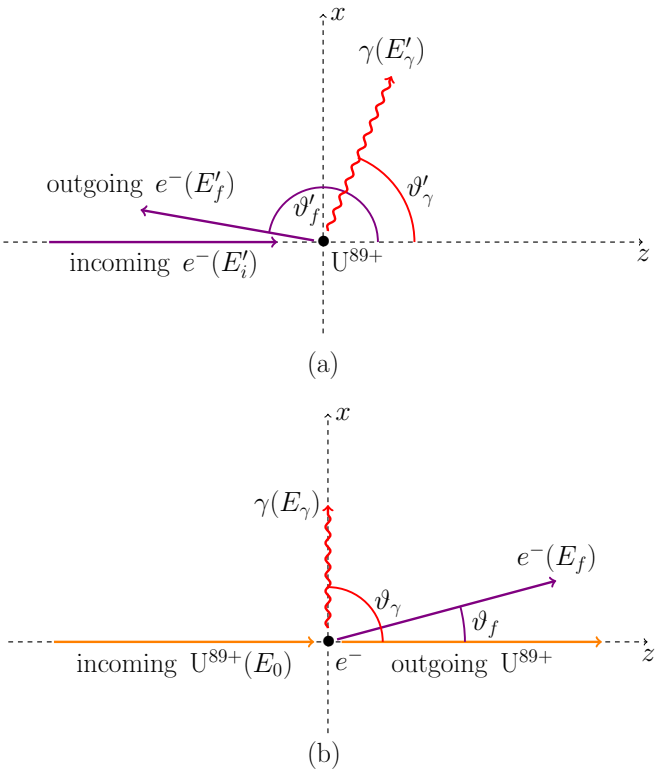

FIG. 1. The kinematics of the reaction as described in Sec. III A.

III. THEORY

A. Kinematics

The kinematics of the reaction is schematically illustrated in Fig. 1. The energy balance of the reaction in the projectile frame is given by

$$E'_f + E'_\gamma = E'_i - \gamma v_p q_z. \quad (2)$$

The initial collision energy is $E'_i = E_0$. The energy of the scattered electron E'_f and the energy of the emitted photon E'_γ in the projectile frame are connected to the corresponding observables in the target frame by Lorentz transformation:

$$E'_f(E_f, \vartheta_f) = E_0 + \gamma E_f - \gamma v_p p_f \cos\vartheta_f,$$
$$E'_\gamma(E_\gamma, \vartheta_\gamma) = \gamma E_\gamma(1 - \beta\cos\vartheta_\gamma). \quad (3)$$

The initial binding energy of the target electron is taken into account through the Compton profile $J(q_z)$, which is the projection of the momentum distribution of the target

electron onto the beam axis z. In the present experiment, we measure the electron distribution as a function of E_f. The Compton profile then leads to a broadening of the photon energy distribution E_γ, and for each measured E_f we integrate over the full distribution of E_γ.

Furthermore, the projectile-frame angles ϑ'_f and ϑ'_γ and the observation angles ϑ_f and ϑ_γ in the target frame are connected by

$$\vartheta'_{f,\gamma} = \pi - \arctan\left[\frac{\sin\vartheta_{f,\gamma}}{\gamma(\cos\vartheta_{f,\gamma} - \beta/\beta_{f,\gamma})}\right], \qquad (4)$$

where $\beta_f = p_f/\gamma m_e c$ and $\beta_\gamma = 1$. The values of β and γ are given in Sec. II A. Note that the transformation includes a rotation by 180°, or equivalently, the reversal of the beam direction. Therefore, electrons observed in the target frame at energies $E_f < E_0$ correspond to forward scattered electrons in the projectile frame, while electrons with $E_f > E_0$ correspond to backward scattered electrons.

B. Triple-differential cross sections

In the projectile frame, triple-differential cross sections $d^3\sigma^{\rm BS}/dE'_f d\Omega'_f d\Omega'_\gamma$ as a function of ϑ'_f and E'_f were calculated using the fully relativistic approach for electron-nucleus bremsstrahlung presented in Refs. [15–17], which comprises the interaction of the electron with the radiation field of the emitted photon in all orders. Furthermore, the cross sections were averaged over the azimuthal angle $\varphi'_f = \varphi_f$. In the calculations, an effective charge of $Z_{\rm eff} = 89$ was used for the Coulomb field of the nucleus.

The distribution of electrons measured within a polar angle of $\vartheta_f = 0° - \vartheta_{\rm max}$ and an azimuthal angle of $\varphi_f = 0° - 360°$ as a function of the emission energy E_f is given by [28]

$$\left.\frac{d^3\sigma^{\rm RECC}}{dE_f d\Omega_f d\Omega_\gamma}\right|_{\vartheta_f=0°} = \frac{Z_{\rm t}}{\gamma^2}\frac{1}{\pi\vartheta^2_{\rm max}}\int_0^{\vartheta_{\rm max}} \sin\vartheta'_f d\vartheta_f \times \int_0^{2\pi} d\varphi_f \frac{d^3\sigma^{\rm BS}(E'_f,\vartheta'_f)}{dE'_f d\Omega'_f d\Omega'_\gamma}. \qquad (5)$$

Here, $E'_f(E_f,\vartheta_f)$ and $\vartheta'_f(E_f,\vartheta_f)$ were calculated through Eqs. (3) and (4), respectively. The factor $Z_{\rm t} = 7$ reflects the number of electrons per nitrogen target atom. The factor $1/\gamma^2 = d\Omega'_\gamma/d\Omega_\gamma$ is the solid angle transformation for photons emitted under $\vartheta_\gamma = 90°$. The factor $\pi\vartheta^2_{\rm max}$ provides the normalization for the solid angle integration of the electron. The value of $\vartheta_{\rm max}$ is discussed in Sec. II B.

The accuracy for the evaluation of Eq. (5) critically depends on the point density of the two-dimensional grid for $d^3\sigma^{\rm BS}/dE'_f d\Omega'_f d\Omega'_\gamma$. In the present calculation, the angular distribution was calculated for $\vartheta'_f = 0°$–$180°$ in steps of 3.6°. The energy distribution was calculated for $E'_f = 1$ eV, and for $E'_f = 1$–20 keV in steps of 1 keV. A subset of the theoretical results is shown in Fig. 2. In all these calculations, the photon emission angle based on Eq. (4) was $\vartheta'_\gamma = 67.6°$. A linear interpolation was applied to the calculated two-dimensional grid of point for E'_f and ϑ'_f in order to perform the transformation of Eq. (5).

The convolution of the electron spectrum with the momentum resolution of the spectrometer, $\Delta p_e/p_e = 2\%$, was found to be negligible for the shape of electron energy distribution on the level of accuracy relevant here, and was therefore omitted in the present analysis.

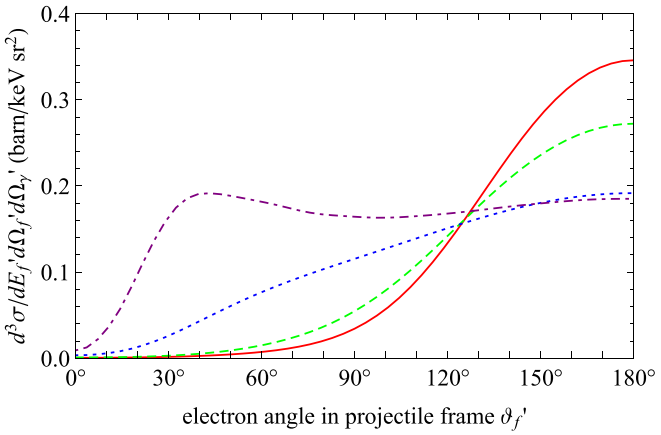

FIG. 2. Electron angular distribution in the projectile frame calculated in the fully relativistic approach [15–17] for incoming electrons of $E'_i = 41.64$ keV, which undergo a bremsstrahlung process with emission of a photon at a polar angle of $\vartheta'_\gamma = 67.6°$. The energy of the scattered electron E'_f was chosen to be 1 eV (solid red line), 1 keV (dashed green line), 10 keV (dotted blue line), and 20 keV (dot-dashed purple line). Shown is the polar angular distribution of ϑ'_f, while the distribution is averaged over the azimuthal angle φ'_f.

IV. RESULTS

A. X-ray spectrum

The x-ray spectrum measured at $\vartheta_\gamma = 90°$ is shown in Fig. 3. The plotted spectrum was corrected for the energy dependency in the x-ray detection efficiency $\epsilon(E_\gamma)$. The x-ray

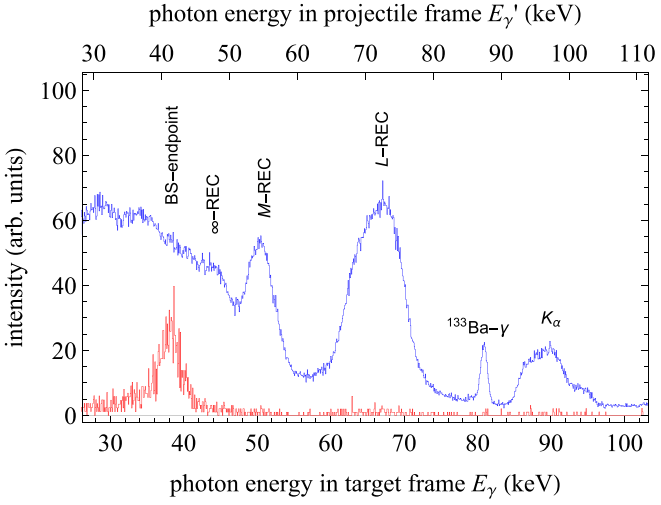

FIG. 3. X-ray energy spectra observed under $\vartheta_\gamma = 90°$ without coincidence condition (upper blue line) and in coincidence with an electron emitted under $\vartheta_f = 0°$ (lower red line). The two spectra were recorded separately, triggered by the x-ray signal and the electron signal, respectively. The coincidence spectrum triggered by the electron signal was summed over all measured values of E_f. See Sec. IV A for labels of peaks.

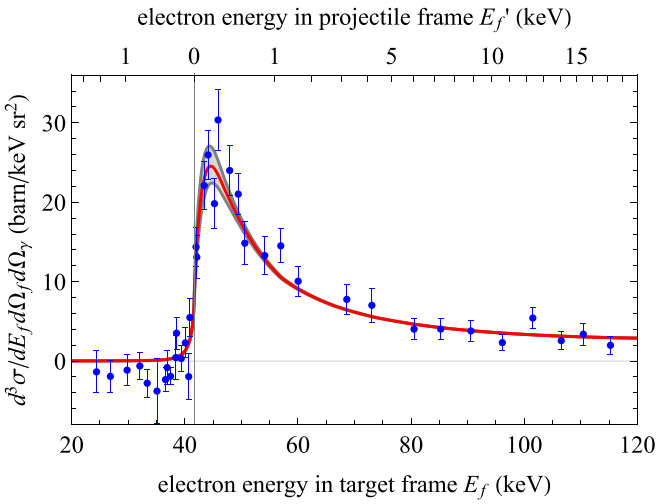

FIG. 4. Electron energy spectrum measured in coincidence with the bremsstrahlung photon (blue data points with statistical error bars). Theory was calculated for different values of $\vartheta_{\max}$: 3.0° (upper gray line), 3.3° (middle red line), and 3.6° (lower gray line). The measurements were normalized to theory by multiplication with a fitted constant.

detector was optimized for a large solid angle $\Delta\Omega_\gamma$, which resulted in a large Doppler broadening of the measured photon energies and a reduced energy resolution.

The spectrum without coincidence conditions is dominated by peaks from radiative electron capture (REC) into the partially unoccupied L shell, into the empty M shell, and into Rydberg states (∞) of the U^{89+} projectile [21]. Furthermore, the characteristic K_α transition lines originating dominantly from relaxation following the $1s^2 2s$-$1s2s2p$ excitation of U^{89+} can be seen. (The ^{133}Ba-γ line originates from a calibration source present near the detector.)

The photon energy spectrum measured in coincidence with the detected electron is summed over all energy settings of the electron spectrometer. The plot illustrates, that the electron-photon coincidence condition has an unambiguous selectivity on events from the high-energy endpoint of the bremsstrahlung spectrum.

B. Electron spectrum

In Fig. 4, the electron energy spectrum measured for the RECC is shown. Based on Eq. (5), the triple-differential cross section is given per nitrogen atom. For the theoretical evaluation of Eq. (5), the electron angular distribution was varied with $\vartheta_{\max} = 3.0° \pm 0.3°$, as motivated in Sec. II B. The maximum of the electron distribution for $\vartheta_{\max} = 3.0°$ and $\vartheta_{\max} = 3.6°$ are 10.3% higher and 8.6% lower than the maximum for $\vartheta_{\max} = 3.3°$, respectively.

The target frame electron energy ranges within $E_f = 20$–120 keV as shown in Fig. 4. The projectile frame energy ranges from the high-energy endpoint of electron-nucleus bremsstrahlung with $E'_f = 0$ keV and $E'_\gamma = E'_i$ signifying full energy transfer from the incoming electron to the emitted photon, to $E'_f = 19$ keV and $E'_\gamma = 0.45 \times E'_i$ signifying a partial energy transfer.

It should be noted that the maximum of the electron distribution is at an energy slightly above E_0. The fact that the probability for electrons being emitted with $E_f < E_0$ is almost negligible has to be attributed to the angular distribution of electron in the underlying bremsstrahlung process in the projectile frame, where forward emission angles $\vartheta'_f < 90°$ are highly suppressed at low emission energies E'_f, as shown in Fig. 2.

C. Discussion

The collision system of this paper is directly comparable to the system studied by Nofal *et al.* [27] and Hillenbrand *et al.* [28], which was U^{88+} colliding with a N_2 target at a projectile energy of 90 MeV/u. At the high-energy endpoint, the bremsstrahlung cross section used in Eq. (5) scales with the effective charge of the nucleus approximately as Z^3_{eff}, and with the incoming electron energy approximately as $E_i'^{-2}$ [2]. Thus, the current collision system offers about 1.5 times larger projectile-frame cross section.

In an attempt to compare the data shown in Fig. 4 with the data of the two previous studies, the current result presents a clear improvement of the agreement between experiment and theory. This improvement originates both from theoretical and experimental aspects. On the theoretical side, the number of grid points calculated for the evaluation of Eq. (5) was significantly increased from 5 values of E'_f used in Ref. [28] to 21 values of E'_f in the present calculation as described in Sec. III. The importance of choosing appropriate grid points can be seen by comparing the values given in Sec. III with the top axis of E'_f in Fig. 4. This aspect previously emphasized by Jakubassa-Amundsen [29] results in a higher numerical accuracy of the theoretical calculations.

On the experimental side, significant improvements on the accuracy of operating the spectrometer were achieved. More specifically, accurately scanning the electron energy was challenging due to the fact that dipole magnets experience hysteresis effects while the iron-free quadrupole triplet does not. Taking the whole data set within one scan from low to high electron energies led to a better stability of the transmission and efficiency across the scanned energy range, minimizing the relative systematic error: In the analysis of Ref. [28] a relative systematic error of 20% was given, while the error bars shown in Fig. 4 are purely statistical. Furthermore, the electron angular acceptance determined by the setting of the quadrupole triplet has been increased and characterized more accurately in the present study, changing from $\vartheta_{\max} = 2.4°$ used in Ref. [28] to $\vartheta_{\max} = 3.3° \pm 0.3°$ in this work. Reanalysis of the data of Ref. [28] showed that a possible underestimation of $\vartheta_{\max}$ in the former work would only partially reduce the discrepancy between experiment and theory.

Finally, it is worth mentioning, that the observed asymmetry of the electron cusp is opposite to that of the nonradiative electron-capture-to-continuum (ECC) cusp: For the case of target electrons captured into the low-energy continuum of the projectile *with* emission of a photon, the electron cusp is dominated by electrons $E_f > E_0$, i.e., faster than the projectile, while for target electrons captured into the low-energy continuum of the projectile *without* emission of a photon,

the electron cusp is dominated by electrons $E_f < E_0$, i.e., slower than the projectile [33]. As has been first discussed in Ref. [34] for the ECC, a cusp shape dominated by electrons with $E_f < E_0$ leads to a behavior, where the maximum of the electron distribution is at an energy below E_0. Analogously, our experimental and theoretical electron distributions of the RECC shown in Fig. 4 have their maximum at an energy slightly above E_0.

V. SUMMARY AND OUTLOOK

In this paper we have presented a measurement of the RECC cusp in collisions of U^{89+} with a N_2 target at a collision energy of 75.91 MeV/u. Compared to previous studies, we find an improved agreement of our experimental data with the fully relativistic theory of electron-nucleus bremsstrahlung up to the high-energy endpoint. This improvement is mainly attributed to the reduction of the experimental systematic uncertainties as well as the increase of the numerical accuracy of theory. Based on the presented experimental and theoretical data and their uncertainties, the shape of the RECC cusp now appears to be well understood, at least for the studied and similar collision systems. Future experimental studies may include the absolute scale of the RECC process, which would probe the value of Z_{eff} for bremsstrahlung of electrons on partially stripped ions, i.e., the partial screening of the Coulomb potential of the ion.

Bearing in mind the shape of the RECC cusp, it can be used as an independent diagnostic tool for further electron cusp studies. For example, the electron energy axis can be calibrated by fitting the measured RECC spectrum to the fully relativistic theory. Here, the large slope in the electron energy distribution around E_0 would lead to in increased accuracy in the energy calibration in comparison to using the rather broad—usually symmetric—ELC cusp for calibration [30]. This is particularly important in collision systems, where asymmetries of the ECC cusp [33] or special cases of collision systems with an asymmetric ELC cusp [35,36] measured in parallel to the RECC are to be studied with high accuracy.

ACKNOWLEDGMENTS

M.E.G. gratefully acknowledges support from the GSI Summer Student Program. E.P.B., E.D.F., and E.V.P. gratefully acknowledge support from the "Transnational Access to GSI" (TNA) activity. C.B. acknowledges support from BMBF Contract No. 05P15RGFAA. M.V. acknowledges support from BMBF Contract No. 05P15SJFAA. This work was supported by the Helmholtz-CAS Joint Research Group HCJRG-108 and ERC Grant No. 682841 "ASTRUm."

[1] H. K. Tseng and R. H. Pratt, Electron Bremsstrahlung from Neutral Atoms, Phys. Rev. Lett. **33**, 516 (1974).
[2] C. M. Lee, L. Kissel, R. H. Pratt, and H. K. Tseng, Electron bremsstrahlung spectrum, 1–500 keV, Phys. Rev. A **13**, 1714 (1976).
[3] U. Fano, H. W. Koch, and J. W. Motz, Evaluation of Bremsstrahlung Cross Sections at the High-Frequency Limit, Phys. Rev. **112**, 1679 (1958).
[4] U. Fano, K. McVoy, and J. Albers, Sauter Theory of the Photoelectric Effect, Phys. Rev. **116**, 1147 (1959).
[5] U. Fano, High-Frequency Limit of Bremsstrahlung in the Sauter Approximation, Phys. Rev. **116**, 1156 (1959).
[6] U. Fano, K. McVoy, and J. Albers, Interference of Orbital and Spin Currents in Bremsstrahlung and Photoelectric Effect, Phys. Rev. **116**, 1159 (1959).
[7] K. W. McVoy and U. Fano, Bremsstrahlung and the Photoelectric Effect as Inverse Processes, Phys. Rev. **116**, 1168 (1959).
[8] R. Pratt, High-Frequency Region of the Bremsstrahlung Spectrum, Phys. Rev. **120**, 1717 (1960).
[9] R. H. Pratt and H. K. Tseng, Tip region of the bremsstrahlung spectrum from incident electrons of kinetic energy 50 keV–1.84 MeV, Phys. Rev. A **11**, 1797 (1975).
[10] R. Jabbur and R. Pratt, High-Frequency Region of the Spectrum of Electron and Positron Bremsstrahlung, Phys. Rev. **129**, 184 (1963).
[11] H. K. Tseng and R. H. Pratt, Exact Screened Calculations of Atomic-Field Bremsstrahlung, Phys. Rev. A **3**, 100 (1971).
[12] H. K. Tseng and R. H. Pratt, Polarization Correlations in Atomic-Field Bremsstrahlung, Phys. Rev. A **7**, 1502 (1973).
[13] C. M. Lee, R. H. Pratt, and H. K. Tseng, Bremsstrahlung spectrum from atomic ions, Phys. Rev. A **16**, 2169 (1977).
[14] H. K. Tseng and R. H. Pratt, Electron bremsstrahlung energy spectra above 2 MeV, Phys. Rev. A **19**, 1525 (1979).
[15] V. A. Yerokhin and A. Surzhykov, Electron-atom bremsstrahlung: Double-differential cross section and polarization correlations, Phys. Rev. A **82**, 062702 (2010).
[16] V. A. Yerokhin, A. Surzhykov, R. Märtin, S. Tashenov, and G. Weber, Comparative study of the electron-atom and positron-atom bremsstrahlung, Phys. Rev. A **86**, 032708 (2012).
[17] R. A. Müller, V. A. Yerokhin, and A. Surzhykov, Polarization of atomic bremsstrahlung in coincidence studies, Phys. Rev. A **90**, 032707 (2014).
[18] R. Märtin, G. Weber, R. Barday, Y. Fritzsche, U. Spillmann, W. Chen, R. D. DuBois, J. Enders, M. Hegewald, S. Hess, A. Surzhykov, D. B. Thorn, S. Trotsenko, M. Wagner, D. F. A. Winters, V. A. Yerokhin, and T. Stöhlker, Polarization Transfer of Bremsstrahlung Arising from Spin-Polarized Electrons, Phys. Rev. Lett. **108**, 264801 (2012).
[19] S. Tashenov, T. Bäck, R. Barday, B. Cederwall, J. Enders, A. Khaplanov, Y. Fritzsche, K.-U. Schässburger, A. Surzhykov, V. A. Yerokhin, and D. Jakubassa-Amundsen, Bremsstrahlung polarization correlations and their application for polarimetry of electron beams, Phys. Rev. A **87**, 022707 (2013).
[20] M. E. Groshev, V. A. Zaytsev, V. A. Yerokhin, and V. M. Shabaev, Bremsstrahlung from twisted electrons in the field of heavy nuclei, Phys. Rev. A **101**, 012708 (2020).
[21] J. Eichler and T. Stöhlker, Radiative electron capture in relativistic ion-atom collisions and the photoelectric effect in hydrogen-like high-Z systems, Phys. Rep. **439**, 1 (2007).
[22] D. H. Jakubassa-Amundsen, Radiative electron capture to continuum in relativistic ion atom collisions, J. Phys. B **36**, 1971 (2003).

[23] D. H. Jakubassa-Amundsen, Bremsstrahlung during electron capture to continuum, Radiat. Phys. Chem. **75**, 1319 (2006).

[24] D. H. Jakubassa-Amundsen, The polarization of bremsstrahlung from radiative ionization induced by relativistic highly charged projectiles, J. Phys. B **40**, 2719 (2007).

[25] D. H. Jakubassa-Amundsen, Competing processes for electron capture to continuum in relativistic ion-atom collisions, Eur. Phys. J. D **41**, 267 (2007).

[26] D. H. Jakubassa-Amundsen, Radiative ionization: The link between radiative electron capture and bremsstrahlung, *Radiation Physics Research Progress* (Novapublishers, New York, 2008), pp. 155–191.

[27] M. Nofal, S. Hagmann, T. Stöhlker, D. H. Jakubassa-Amundsen, C. Kozhuharov, X. Wang, A. Gumberidze, U. Spillmann, R. Reuschl, S. Hess, S. Trotsenko, D. Banas, F. Bosch, D. Liesen, R. Moshammer, J. Ullrich, R. Dörner, M. Steck, F. Nolden, P. Beller, H. Rothard, K. Beckert, and B. Franczak, Radiative Electron Capture to the Continuum and the Short-Wavelength Limit of Electron-Nucleus Bremsstrahlung in 90 AMeV $U^{88+}(1s^2 2s^2) + N_2$ Collisions, Phys. Rev. Lett. **99**, 163201 (2007).

[28] P.-M. Hillenbrand, S. Hagmann, D. Atanasov, D. Banas, K.-H. Blumenhagen, C. Brandau, W. Chen, E. De Filippo, A. Gumberidze, D. L. Guo, D. H. Jakubassa-Amundsen, O. Kovtun, C. Kozhuharov, M. Lestinsky, Y. A. Litvinov, A. Müller, R. A. Müller, H. Rothard, S. Schippers, M. S. Schöffler, U. Spillmann, A. Surzhykov, S. Trotsenko, N. Winckler, X. L. Yan, V. A. Yerokhin, X. L. Zhu, and T. Stöhlker, Radiative-electron-capture-to-continuum cusp in $U^{88+} + N_2$ collisions and the high-energy endpoint of electron-nucleus bremsstrahlung, Phys. Rev. A **90**, 022707 (2014).

[29] D. Jakubassa-Amundsen, R. Müller, A. Surzhykov, and V. Yerokhin, Relativistic theory for radiative forward electron emission in heavy ion-atom encounters, Eur. Phys. J. D **68**, 367 (2014).

[30] P.-M. Hillenbrand, S. Hagmann, A. B. Voitkiv, B. Najjari, D. Banas, K.-H. Blumenhagen, C. Brandau, W. Chen, E. De Filippo, A. Gumberidze, D. L. Guo, C. Kozhuharov, M. Lestinsky, Y. A. Litvinov, A. Müller, H. Rothard, S. Schippers, M. S. Schöffler, U. Spillmann, S. Trotsenko, X. L. Zhu, and T. Stöhlker, Electron-loss-to-continuum cusp in $U^{88+} + N_2$ collisions, Phys. Rev. A **90**, 042713 (2014).

[31] D. Schneider, W. Zeitz, R. Kowallik, G. Schiwietz, T. Schneider, N. Stolterfoht, and U. Wille, Effects of external electric fields on high Rydberg states formed in foil and gas interactions of 85-MeV Ne^{6+} ions, Phys. Rev. A **34**, 169 (1986).

[32] B. D. DePaola, Y. Kanait, P. Richard, Y. Awaya, H. Schöne, J. M. Sanders, J. P. Giese, and T. J. M. Zouros, Stark beats from highly charged Rydberg ions created in high-energy beam-foil collisions, J. Phys. B **29**, 1247 (1996).

[33] P.-M. Hillenbrand, S. Hagmann, D. H. Jakubassa-Amundsen, J. M. Monti, D. Banas, K.-H. Blumenhagen, C. Brandau, W. Chen, P. D. Fainstein, E. De Filippo, A. Gumberidze, D. L. Guo, M. Lestinsky, Y. A. Litvinov, A. Müller, R. D. Rivarola, H. Rothard, S. Schippers, M. S. Schöffler, U. Spillmann, S. Trotsenko, X. L. Zhu, and T. Stöhlker, Electron-capture-to-continuum cusp in $U^{88+} + N_2$ collisions, Phys. Rev. A **91**, 022705 (2015).

[34] M. B. Shah, C. McGrath, C. Illescas, B. Pons, A. Riera, H. Luna, D. S. F. Crothers, S. F. C. O'Rourke, and H. B. Gilbody, Shifts in electron capture to the continuum at low collision energies: Enhanced role of target postcollision interactions, Phys. Rev. A **67**, 010704(R) (2003).

[35] P.-M. Hillenbrand, S. Hagmann, J. M. Monti, R. D. Rivarola, K.-H. Blumenhagen, C. Brandau, W. Chen, R. D. DuBois, A. Gumberidze, D. L. Guo, M. Lestinsky, Y. A. Litvinov, A. Müller, S. Schippers, U. Spillmann, S. Trotsenko, G. Weber, and T. Stöhlker, Strong asymmetry of the electron-loss-to-continuum cusp of multielectron U^{28+} projectiles in near-relativistic collisions with gaseous targets, Phys. Rev. A **93**, 042709 (2016).

[36] K. N. Lyashchenko, O. Y. Andreev, and A. B. Voitkiv, Electron loss from hydrogen-like highly charged ions in collisions with electrons, protons and light atoms, J. Phys. B **51**, 055204 (2018).